ACS APPLIED MATERIALS & INTERFACES

Research Article

Cite This: ACS Appl. Mater. Interfaces 2019, 11, 5325−5335

www.acsami.org

Biomimetic Carbon Fiber Systems Engineering: A Modular Design Strategy To Generate Biofunctional Composites from Graphene and Carbon Nanofibers

Mohammadreza Taale,[†] Fabian Schütt,[‡] Tian Carey,[§] Janik Marx,[∥] Yogendra Kumar Mishra,[‡] Norbert Stock,[⊥] Bodo Fiedler,[∥] Felice Torrisi,[§] Rainer Adelung,[‡] and Christine Selhuber-Unkel*[,†]

[†]Biocompatible Nanomaterials, Institute for Materials Science and [‡]Functional Nanomaterials, Institute for Materials Science, Kiel University, Kaiserstraße 2, D-24143 Kiel, Germany

[§]Cambridge Graphene Centre, University of Cambridge, 9 JJ Thomson Avenue, Cambridge CB3 0FA, U.K.

[∥]Institute of Polymer and Composites, Hamburg University of Technology, Denickestraße 15, D-21073 Hamburg, Germany

[⊥]Institute of Inorganic Chemistry, Kiel University, Max-Eyth Straße 2, D-24118 Kiel, Germany

Supporting Information

ABSTRACT: Carbon-based fibrous scaffolds are highly attractive for all biomaterial applications that require electrical conductivity. It is additionally advantageous if such materials resembled the structural and biochemical features of the natural extracellular environment. Here, we show a novel modular design strategy to engineer biomimetic carbon fiber-based scaffolds. Highly porous ceramic zinc oxide (ZnO) microstructures serve as three-dimensional (3D) sacrificial templates and are infiltrated with carbon nanotubes (CNTs) or graphene dispersions. Once the CNTs and graphene coat the ZnO template, the ZnO is either removed by hydrolysis or converted into carbon by chemical vapor deposition. The resulting 3D carbon scaffolds are both hierarchically ordered and free-standing. The properties of the microfibrous scaffolds were tailored with a high porosity (up to 93%), a high Young's modulus (ca. 0.027−22 MPa), and an electrical conductivity of ca. 0.1−330 S/m, as well as different surface compositions. Cell viability, fibroblast proliferation rate and protein adsorption rate assays have shown that the generated scaffolds are biocompatible and have a high protein adsorption capacity (up to 77.32 ± 6.95 mg/cm^3) so that they are able to resemble the extracellular matrix not only structurally but also biochemically. The scaffolds also allow for the successful growth and adhesion of fibroblast cells, showing that we provide a novel, highly scalable modular design strategy to generate biocompatible carbon fiber systems that mimic the extracellular matrix with the additional feature of conductivity.

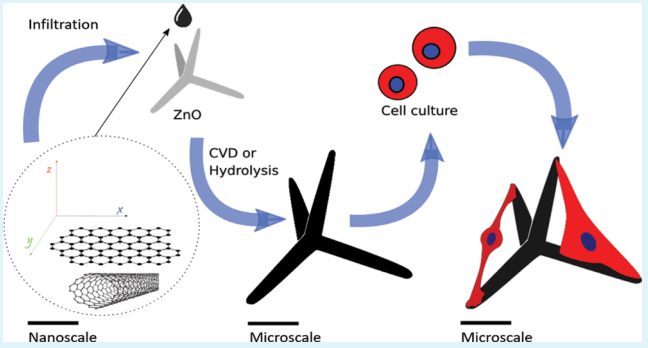

KEYWORDS: *tissue engineering, CNT, graphene, aerographite, ZnO, three-dimensional scaffold, cell adhesion*

1. INTRODUCTION

Regenerative medicine aims at developing microenvironments for the regrowth of damaged or dysfunctional tissue and organs. New promising strategies of regenerative medicine make use of biomaterial scaffolds that resemble the chemical composition,[1] the topographical structure, and the three-dimensional (3D) micro- and nanoenvironments of extracellular matrix (ECM).[2] The ECM consists of interwoven protein fibers, such as collagens, in different ranges of diameters varying from a few (<5 nm) up to several hundred nanometers for bundled collagen fibrils.[3] The chemical, structural, and mechanical features of the ECM significantly control cell migration, as well as tissue development and maintenance[4] such that finding novel ways to mimic the ECM is a highly important task in biomaterials science. As the diameter (<5 nm) and length (<500 nm) of unbundled collagen fibrils are in the range of those of carbon nanotubes (CNTs),[3] CNTs present an interesting substitute for collagen fibrils.

A general goal of artificially fabricated biomaterial scaffolds is to promote cells to differentiate and proliferate in three dimensions so that they fulfill their functions in the artificial tissue and integrate well after implantation.[5] Particularly, the microstructure and porosity of a scaffold are the key to achieve spatially organized cell growth, besides the induction of specific biological functions in the regenerated tissue. Tailoring pore size, shape, and interconnectivity of a scaffold ensures that cell migration, as well as oxygen and nutrient contribution are similar to the conditions of natural tissues.[6] Often, a large pore size in

Received: October 11, 2018
Accepted: January 2, 2019
Published: January 2, 2019

DOI: 10.1021/acsami.8b17627
ACS Appl. Mater. Interfaces 2019, 11, 5325−5335

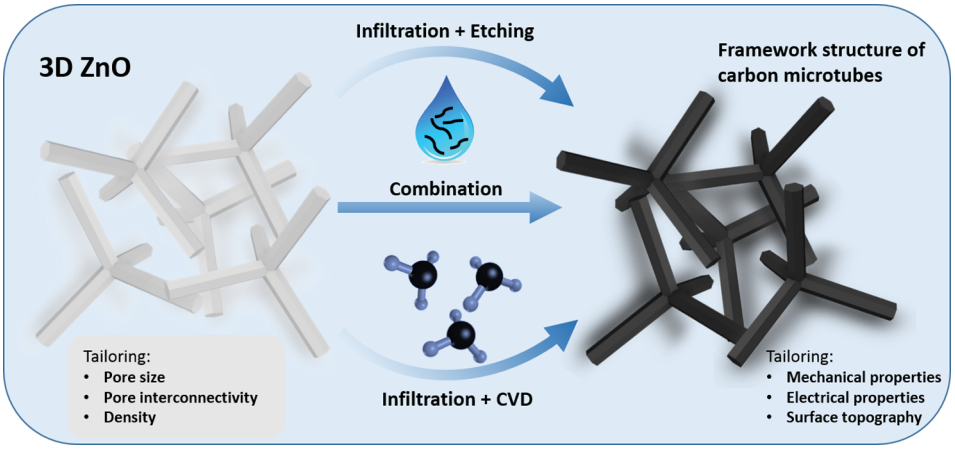

Figure 1. Schematic illustration of different 3D carbon tube structures. The highly porous ZnO template can be either infiltrated with a nanoparticle dispersion (e.g., graphene, CNT) leading to a homogeneous coating around the tetrapodal particles or converted to a graphitic structure using a chemical vapor deposition (CVD) process (aerographite). The combination of both processes leads to a modular design strategy, especially in terms of conductivity, mechanical stiffness, and surface topography.

the range of a few micrometers supports cell migration and ensures the transport of nutrition and waste products.[7]

In neural implants and heart tissue engineering, the electrical conductivity of a scaffold material is often a further requirement necessary for cellular signaling and function.[8] For example, conductivities of 0.03−0.6 S/m have been reported for cardiac muscles.[9] Carbon-based nanomaterials can in principle fulfill such requirements for 3D assemblies.[10,11] CNTs have a high electrical conductivity (up to 67 000 S/cm)[12] and chemical stability (e.g., against acids);[13] while graphene (G) offers high surface area (2630 m^2/g)[14] and high electrical conductivity (10^7−10^8 S/m).[15] Both CNTs and graphene have attracted significant attention in biomedical applications, ranging from biosensors[16] and drug/gene delivery[17] to targeted bioimaging.[17] In addition, compared to other carbon-based nanomaterials, the high physical aspect ratio of CNTs (up to 3750 length/diameter) and graphene provides a sufficient surface area for the attachment of adhesion ligands and cells.[14,18] Regarding neural tissue engineering, 3D graphene foams[19] and graphene films[18] have contributed to enhance neural stem cell differentiation toward astrocytes and neurons.[20]

An important requirement for such carbon-containing scaffolds is biocompatibility. The biocompatibility of CNTs depends on the concentration of CNTs,[21] their degree of purification, synthesis method,[22] aspect ratio, diameter and number of CNT walls,[23] and their surface functionalization.[24] Although many studies have proven the feasibility of CNTs as biocompatible material,[25] the cytotoxicity of CNTs is still a concern due to residual metal catalysts, amorphous carbon, and CNT aggregation that can occur within the cell.[26] In contrast, graphene has been reported to be biocompatible and is readily applicable for a variety of biological applications, including the use of neuronal cells,[18] cardiomyocytes,[27] and osteoblast[28] cells. Graphene oxide (GO) is an interesting graphene derivative, as it consists of a single atomic carbon layer decorated with hydrophilic functional groups such as carboxylic acid, hydroxyl, and epoxide.[29] In particular, GO has shown a strong tendency to interact with peptides and proteins via physical or chemical bonds.[30] Therefore, graphene and GO have great potential in biomedical applications as they can easily be converted into biofunctional, peptide- or protein-coated surfaces. Moreover, carbon microtube materials, specifically aerographite (AG), are of further interest as biomaterials due to their electrical conductivity (0.2−0.8 S/m)[31] and highly porous (up to 99.99%)[32] 3D interconnected network. A recent study has demonstrated the feasibility of AG as a suitable 3D matrix for cell migration and proliferation.[33] However, a clear pathway to generate a highly porous biocompatible ECM-mimetic scaffold with tunable porosity, electrical conductivity, and suitable mechanics for biomedical applications has so far been missing.

Here we demonstrate a novel modular design strategy to generate hierarchically structured carbon-based, microfibrous scaffold materials with adjustable electrical and mechanical properties that mimic the structure of the extracellular matrix. The materials investigated here are biocompatible, support cell proliferation and adhesion, and open the gateway to future biomaterial development, where biocompatibility and electrical conductivity are vital for cell proliferation and stimulation.

2. RESULTS AND DISCUSSION

2.1. Novel Types of Graphitic Scaffolds by CNT and Graphene Infiltration. Different types of fibrous 3D carbon scaffolds have been prepared based on our modular template-mediated method. Figure 1 shows the modular design strategy of our fabrication method. The fabrication uses presintered highly porous (porosity > 93%) ceramic ZnO templates as a sacrificial material.[32] These ZnO templates themselves consist of interconnected tetrapod-shaped ZnO particles. Representative scanning electron microscopy (SEM) images of the ZnO templates are shown in the Supporting Information Figure S2. The highly porous ZnO templates have an interstitial space of approximately 10−100 μm between ZnO filaments, which in turn have diameters between 0.5 and 5 μm. Therefore, the spatial geometry and organization of the microtube-shaped structures of the ZnO template are comparable to that of the ECM.[34]

The coating of ZnO templates with carbon nanomaterials (e.g., CNTs, graphene) is performed via a simple process to infiltrate the entire 3D template with a CNT dispersion as described by Schütt et al.[35] In addition, here we demonstrate that the feasibility of this technique can be extended also to graphene dispersions. The infiltration process relies on the superhydrophilicity of the ZnO template,[36] which is a direct result of the combination of the hydrophilic character of the

DOI: 10.1021/acsami.8b17627
ACS Appl. Mater. Interfaces 2019, 11, 5325−5335

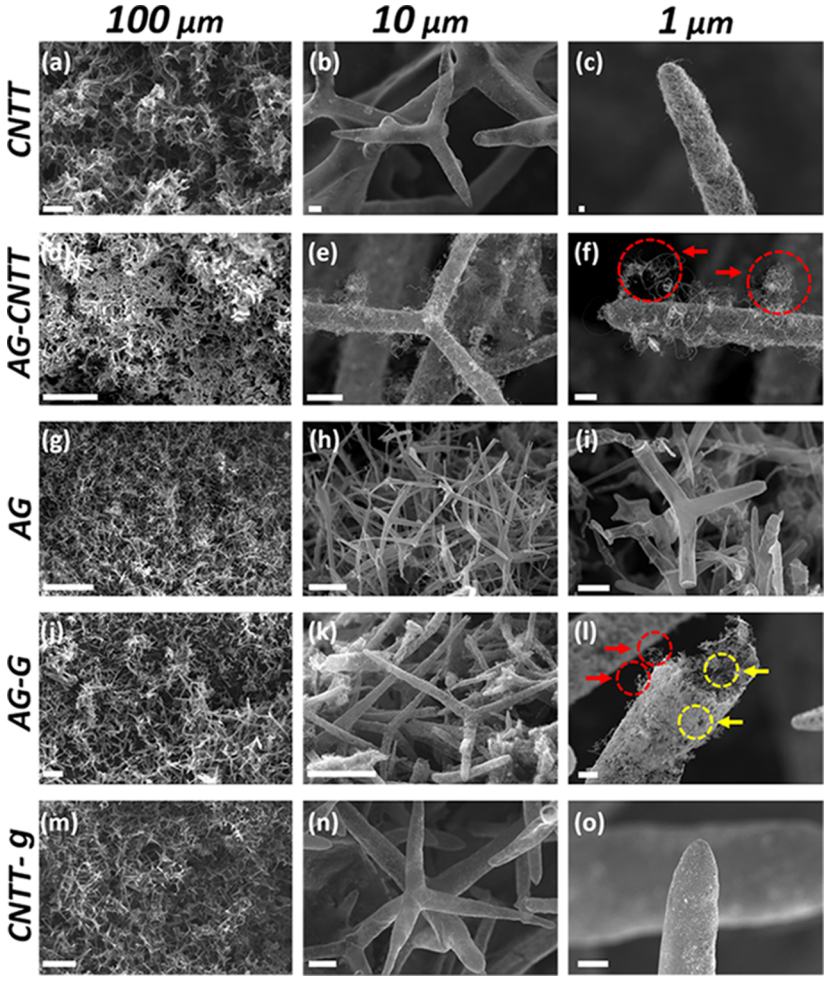

Figure 2. SEM images from low to high magnification of the different 3D carbon structures. (a–c) Carbon nanotube tubes (CNTTs), (d–f) aerographite with incorporated CNTs (AG–CNTT) (the red arrows show the grown CNTs during the CVD process), (g–i) aerographite (AG), (j–l) aerographite with incorporated graphene (AG–G) (the yellow arrows point to nanopores on the surface of aerographite), and (m–o) carbon nanotube tubes incorporated into a thick carbon layer (CNTT–g).

individual tetrapod-shaped ZnO microparticles and the high porosity (>93%) of the template. During water evaporation, the nanomaterials form a widely homogeneous coverage[35] around the ZnO microrods (Supporting Information Figures S3 and S4). The amounts of CNTs and graphene flakes covering the ZnO template can be controlled by cyclically repeating the infiltration process several times (Supporting Information, Figures S3 and S4). SEM images revealed that the infiltrated CNTs form a layer made of self-entangled CNTs around the ZnO network (Supporting Information Figure S4). Similarly to CNTs, a dispersion of graphene flakes also forms a homogeneous layer around the ZnO (Supporting Information Figure S3).

To generate freestanding scaffolds from the ZnO templates after coating them with carbon nanomaterials, the ZnO must be carefully removed. We have used three different processes to remove the sacrificial ZnO network after infiltration (Figure 1): (i) hydrolyzing the sacrificial ZnO template by a HCl solution[35] (Supporting Information Figure S5a), (ii) converting the ZnO template via a CVD process[31] (Supporting Information Figure S5b,c), and (iii) using a carbothermal reduction process[37] in combination with glucose (g) as a carbon source. Each of these processes leads to a specific type of carbon-based scaffold. Therefore, the results of these processes (Supporting Information Figure S5) are discussed in the following sections.

2.2. Freestanding Carbon Nanotube Network (CNTT) Scaffolds from Hydrolysis of the Sacrificial ZnO Template by HCl. When HCl is used to dissolve the ZnO in CNT-coated ZnO templates, hierarchically structured CNTT scaffolds are formed. These structures consist of interconnected hollow tubes, which are composed of self-entangled CNT networks, as reported previously.[35] SEM images of the resulting CNTT scaffolds are presented in Figure 2a–c. The presented structures demonstrate a hierarchical architecture, where the porous scaffold are composed of microtetrapods (Figure 2a,b), which in turn consist of nanoscale CNTs (Figure 2c). The HCl-based ZnO dissolution can only be applied for templates infiltrated with CNTs. Templates infiltrated with graphene only led to collapsing structures (data not shown), presumably as the graphene flakes cannot interweave.

2.3. ZnO Conversion to AG via CVD Forms Composites with Embedded Nanoparticles. We also use a CVD process to remove the ZnO, resulting in a thin (~15 nm) film of graphite around the entire template similar to the graphitic shells in AG.[31] The CVD process can be applied if the ZnO is coated with either CNTs or graphene (Supporting Information Figure S6). Then, the AG serves as an additional backbone. This is the case in all of

DOI: 10.1021/acsami.8b17627
ACS Appl. Mater. Interfaces 2019, 11, 5325–5335

our CVD-based scaffolds, i.e., in composites of graphene and aerographite (AG−G) and in composites of multiwalled CNTs and aerographite (AG−CNTT) (Figure 2d−l). The modular design of the fabrication process allows us to change and tailor the surface topography of the hollow graphitic microtubes. Up to 5 μm long CNTs are formed perpendicular to the surface of microtubes on AG−G and AG−CNTT during the CVD process (Figure 2f). Such CNTs are not formed on pure AG (Figure 2i).[31] The growth of new carbon nanotubes on AG−G networks (Figure 2l, red arrows) is most likely attributed to the adsorption of carbon atom clusters on the active sites of the graphene surface during the CVD process.[38]

2.4. Carbothermal Reduction Process Leads to Novel Types of Graphitic Structures with Embedded CNTs. In the carbothermal reduction reaction,[37] glucose acts as the carbon source enabling the reduction of ZnO in a quartz tube furnace at 950 °C under argon atmosphere. To do so, ZnO templates were infiltrated with a mixture of glucose and CNTs. The carbothermal reduction of ZnO to Zn(g)[37] leads to ZnO removal and to the formation of graphitic shells, thus resulting in the so-called CNTT−g structure (Figure 2m−o). We have confirmed the removal of ZnO by Raman spectroscopy (Figure 3, CNTT−g graph) (see next paragraph). Furthermore, this

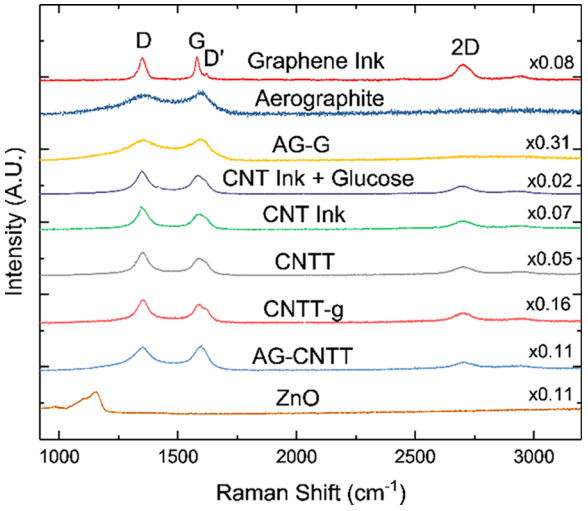

Figure 3. Raman spectroscopy of aerographite, ZnO, CNTT, AG−CNTT, CNTT−g, AG−G, graphene, and CNT inks.

process results in a scaffold with a microstructure that is comparable to that of the AG−CNTT scaffold (Figure 2e,n). However, the graphitic shells of the CNTT−g scaffold appear to be thicker than those of the AG−CNTT scaffold (Figure 2n,o). Additionally, in contrast to the AG−CNTT structures, no additional CNTs are grown (Figure 2n) in the CNTT−g case.

Figure 3 shows Raman spectra (Renishaw 1000 InVia) of all of the carbon-based structures. Raman spectroscopy is used to examine the structural fingerprint of each material at a wavelength of 514.5 nm with an incident power of ∼0.1 mW. The graphene and CNT inks were drop-cast onto Si/SiO_2 substrates before measurement. For the graphene ink (red curve), the G peak (∼1586) corresponds to the E_{2g} phonon at the Brillouin zone center, and the D peak located at ∼1350 cm^{-1} corresponds to the breathing modes of the sp^2 carbon atoms and requires a defect for its activation.[39] Our graphene inks are produced by liquid-phase exfoliation; therefore we attribute this peak to edge defects rather than to defects in the basal plane.[40] The two-dimensional (2D) peak located at ∼2700 cm^{-1} is the D peak overtone and can be fitted by a single Lorentzian, indicating electronically decoupled graphene monolayers.[41]

The aerographite (dark blue curve) shows a G peak position Pos(G) ∼ 1600 cm^{-1} and the absence of a distinct 2D peak, indicating the more defective nature of this sample and a lack of structural order in the aerographite.[42] The AG−G (yellow curve) structure has a similar spectrum to that of aerographite with D and G peaks located at ∼1350 and ∼1600 cm^{-1}, respectively, indicating that the material is mostly composed of aerographite and graphene, given the selective etching of the ZnO scaffold during the CVD reduction.[31] The spectra of the CNT ink (green curve) and CNT ink with glucose (purple curve) show D, G, and 2D peaks at ∼1350, ∼1580, and ∼2700 cm^{-1}, respectively. The peaks from the glucose residue are too weak to be observed. Moreover, the CNTT spectra (gray curve), AG−CNTT (blue curve), and CNTT−g (pink curve) have D, G, and 2D peaks that demonstrate the presence of the CNTs, respectively. Finally, the ZnO spectra (brown curve) display several peaks below 1200 cm^{-1}, predominately created from the intense peak at 1158 cm^{-1} attributed to the $2A_1(LO)$ and $2E_1(LO)$ modes at the Brillouin zone center.[43] However, no peaks attributed to ZnO are observed in any of the CNTTs or aerographite scaffolds, proving the complete removal of the ZnO template.

2.5. Scaffold Mechanics can be Tailored Over Several Orders of Magnitudes. Figure 4 shows Young's moduli and

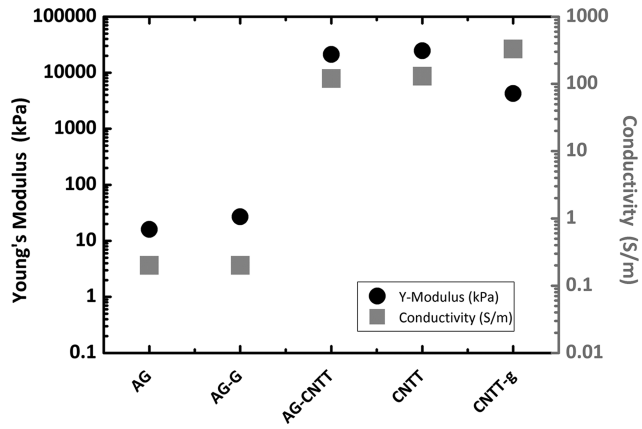

Figure 4. Young's modulus (measured under compression) and electrical conductivity of the 3D CNTT, AG−CNTT, CNTT−g, and AG−G scaffolds. All structures containing CNTs have a higher Young's modulus and conductivity compared to those without CNTs. The values for pure AG and CNTTs were taken from the corresponding publications,[31,35] whereas the other values were measured using a self-built electromechanical testing setup.

electrical conductivities of CNTT, AG−CNTT, CNTT−g, AG, and AG−G. The scaffold with the lowest stiffness is AG with a Young's modulus of 16 kPa, which is comparable to previously reported values.[31] AG−G has a Young's modulus of up to 27 kPa, thus adding graphene into the graphitic shells of AG results in a mechanical reinforcement of the scaffold (∼170%). This reinforcement is in a similar range to that of other graphene-reinforced porous networks, e.g., graphene/chitosan composites[44] (∼200%). In contrast to AG−G, AG−CNTT is much stiffer (Figure 4), with Young's modulus reaching ∼22 MPa.

This reinforcement by a factor of about 1000 is presumably due to the reinforcement of CNTs on the nanoscale by self-

DOI: 10.1021/acsami.8b17627
ACS Appl. Mater. Interfaces 2019, 11, 5325−5335

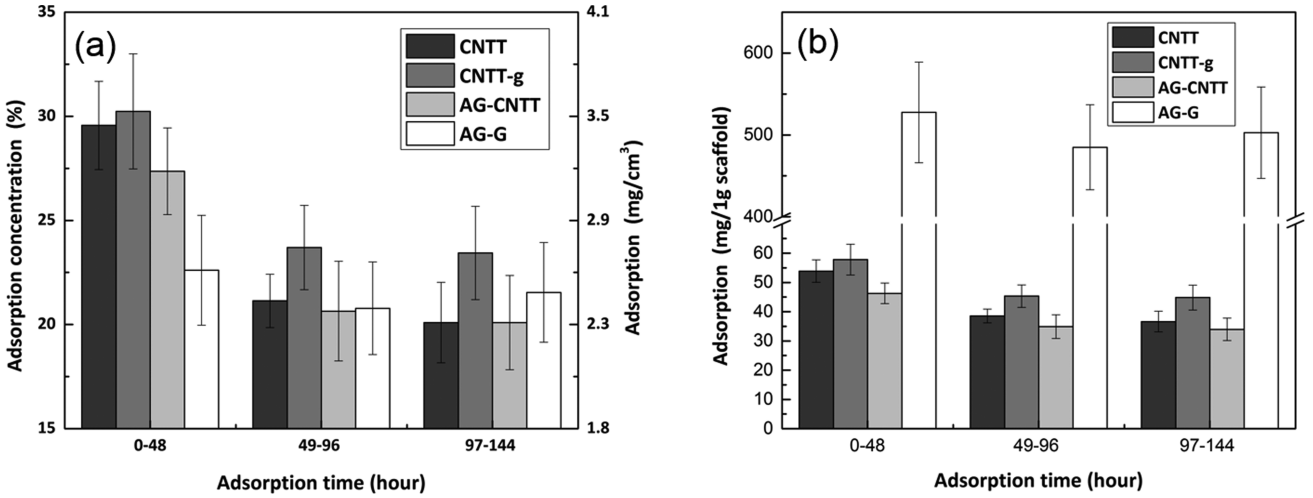

Figure 5. Protein adsorption on CNTT, AG−CNTT, CNTT−g, and AG−G during 0−48, 49−96, and 97−144 h of incubation with albumin solution (1 mg/mL). (a) Absolute protein adsorption amount per scaffold volume. (b) Absolute protein adsorption amount per scaffold weight.

Table 1. Full Names and Abbreviations of Fabricated Materials and Scaffolds in Our Study

full name	abbreviation	density (g/cm^3)	porosity (%)
aerographite	AG	~200 × 10^{-6} [31]	up to ~99.9[31]
carbon nanotube tube	CNTT	~0.064	~94
carbon nanotube tube−glucose	CNTT−g	~0.061	~90
aerographite−carbon nanotube tube	AG−CNTT	~0.069	~95
aerographite−graphene	AG−G	~0.005	~96

entanglement.[35] Hence, the mechanical reinforcement of AG by CNTs is higher than in other CNT-reinforced porous biomaterials, including gelatin methacrylate (GelMA)−CNT composites[45] and poly(propylenefumarate)−CNT composites.[46] Young's modulus of CNTT−g (~4 MPa) is in between the moduli of AG−G and AG−CNTT. These results confirm that the incorporation of CNTs and graphene into 3D scaffolds compensates for the typically low mechanical Young's moduli of porous structures[47] and that AG provides a stable backbone for CNTT scaffolds. In addition, the structural integrity of AG−G scaffolds is demonstrated during a long-cycle compression test (Figure S7) (Supporting Information Video S1).

2.6. Tailoring Scaffold Conductivity. We also investigated the electrical properties of our scaffolds (Figure 4, gray squares). AG−G and AG have similar electrical conductivities of around 0.5 and 0.2 S/m, whereas the conductivities of AG−CNTT and CNTT−g are about 120 and 130 S/m, respectively (Figure 4). Hence, AG−CNTT and CNTT−g clearly have higher electrical conductivities than CNT-containing electrospun fibrous composites (3.5 S/m),[48] which are applied in cardiac tissue engineering. The increase in conductivity of the scaffolds can be mainly attributed to the high conductivity of CNTs that are embedded in the graphitic shells of AG. This effect is more pronounced in the case of AG−CNTT and CNTT−g, presumably as a result of the conductive pathways formed by the self-entangled CNT networks. It has already been shown that by adjusting the CNT concentration during the infiltration process, the conductivity of CNTT can be tailored between 10^{-6} and 130 S/m.[35] Indeed, CNTT−g has the highest conductivity (330 S/m) of our scaffolds.

2.7. Scaffolds Strongly Adsorb Proteins. Albumin is an adhesive protein in plasma and can non-specifically bind to low-dimensional carbon-based materials via electrostatic interactions.[49] Therefore, we checked the albumin adsorption capacity of the scaffolds using the bicinchoninic acid (BCA) assay. As shown in Figure 5, within the first 48 h, albumin adsorption is smaller on AG−G than on AG−CNTT, whereas its adsorption is very similar on all scaffolds later on. The highest absolute protein adsorption mass (30.23−22.6 ± 2.76 mg/cm^3) was detected during the first 2 days of incubation, and the adsorption amount reduced to approximately two-thirds (23.69−20.64 ± 2.39 mg/cm^3) during the third to fourth day of incubation. Overall, protein adsorption is very similar on all tested scaffolds, although CNTT, CNTT−g, and AG−CNTT scaffolds adsorb slightly higher protein amounts (CNTT−g: 77.32 ± 6.95 mg/cm^3; CNTT: 70.77 ± 5.33 mg/cm^3; AG−CNTT: 68.08 ± 6.73 mg/cm^3) than AG−G (64.92 ± 7.2 mg/cm^3) (Figure 5a). This might be attributed to the higher protein adsorption capacity of CNTs than graphene flakes due to van der Waals forces and electrostatic interactions.[30]

To compare our results of protein adsorption with other studies, we needed to relate them to the weight of the scaffolds by taking into account their density (Table 1). Figure 5b shows that protein adsorption per weight of CNTT, CNTT−g, and AG−CNTT scaffolds is different for different scaffold types (CNTT−g: 147.9 ± 13.42 mg/g; CNTT: 128.9 ± 9.69 mg/g; AG−CNTT: 115.14 ± 11.38 mg/g). It is also higher than on single-walled CNTs and graphene (~100 mg/g)[30] and on nanoporous silica (~70 mg/g).[50] In addition, due to its low density, AG−G adsorbs even more protein per weight (1512.25 mg/g) after 144 h, e.g., about 10 times more than our other scaffolds. The albumin adsorption on AG−G even after 48 h (527 mg/g) is comparable to that of graphene oxide (~500 mg/g).[30]

2.8. Biocompatibility of the Carbon-Based Scaffolds. Biocompatibility of the scaffolds is investigated by methylthiazolyldiphenyl-tetrazolium bromide (MTT) metabolic activity and WST-1 assays, as well as by proliferation studies. Figure 6

DOI: 10.1021/acsami.8b17627
ACS Appl. Mater. Interfaces 2019, 11, 5325−5335

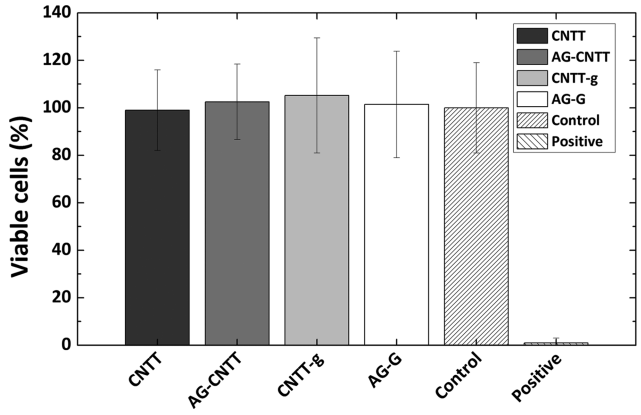

Figure 6. Percentage of viable cells (rat embryonic fibroblasts wild type, REF52wt) relative to the negative control, as determined in an MTT assay (four independent experiments, five technical repeats in each of them). The error bars denote standard deviation.

shows the results for CNTT, CNTT−g, AG−CNTT, and AG−G samples using an MTT assay, demonstrating that all scaffolds are biocompatible, hosting a similar number of viable cells as the negative control. As cell adhesion is not possible on pristine AG without functionalization,[33] biocompatibility of AG is not investigated again in this study.

Figure 7 shows the proliferation rate of rat embryonic fibroblast cells (REF52wt) cultured on CNTT, CNTT−g, AG−

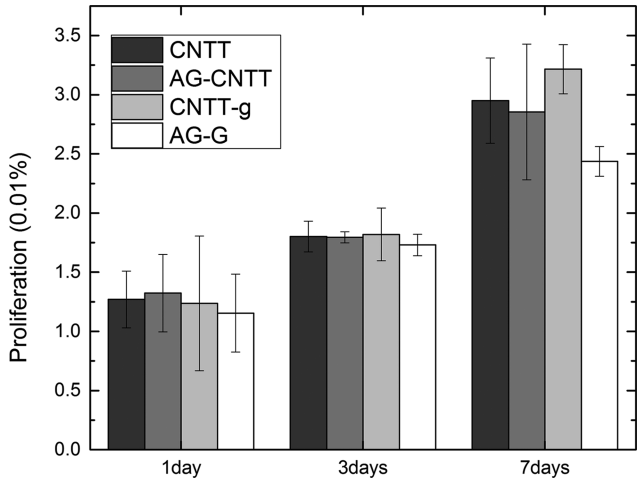

Figure 7. Results of WST-1 metabolic tests of cell proliferation rate (REF52wt). Mean values were determined from four independent experiments, each including five technical repeats. The error bars denote standard deviation, the raw data were normalized to the control, and a correction factor was applied to account for unspecific adsorption (see Materials and Methods).

CNTT, and AG−G samples relative to cells cultured on a culture dish. CNT-containing scaffolds (CNTT, CNTT−g, and AG−CNTT) lead to higher proliferation rates (ca. 300−320%) than graphene-containing structures (AG−G) (~240%) after 7 days in culture. As fibroblast proliferation depends on matrix stiffness,[51] an increase in stiffness might also lead to an increase in fibroblast proliferation,[52] which can be attributed to the translation of mechanical cues from the matrix into a biochemical one via mechanosensory receptors such as focal adhesions.[53] Specifically, it has been reported that fibroblasts need substrates with a minimum Young's modulus of 20−30 kPa to spread and 2 MPa to spread and polarize perfectly.[51] Hence, the huge difference in Young's moduli between CNT-reinforced scaffolds (between 4 MPa in CNTT−g and 23 MPa in CNTT) and graphene-reinforced scaffolds (27 kPa in AG−G) can explain the higher proliferation rate of fibroblast cells on CNTT, AG−CNTT, and CNTT−g compared to AG−G.

2.9. Carbon-Based Scaffolds as Porous Structures for Cell Growth. Fibroblast cells (REF52wt) were cultured for 7 days on the scaffolds to investigate cellular growth at the surface and inside. SEM images of critically point-dried cells (Figure 8) revealed that cells (highlighted in green) are attached to the surface of the scaffolds. Fibroblasts do not migrate strongly within a 3D network[54] but proliferate so that we typically observe several cells at one location. Cells are sprawled and elongated between the filaments of scaffolds and have a polygonal shape on all four scaffold types. Close-up images on the adhesion sites reveal tightly anchored membranes of cells to CNTs and graphene on the surface of structures, comparable to fibroblasts on AG functionalized with cyclic arginylglycylaspartic acid (RGD) peptides.[33]

To investigate cell adhesion at the molecular level, we studied the presence of paxillin in adhesion structures. Paxillin is a component of focal adhesion clusters;[55] therefore, it can be assumed that more paxillin in contact with our scaffolds is related to stronger cell adhesion. We used cells that were stably transfected with yellow fluorescent protein (YFP)-paxillin and imaged the paxillin in fluorescence microscopy. Imaging fluorescence in 3D matrices compared to 2D is challenging.[56] Due to the low intensity of paxillin in the cells and the high light absorbance of our scaffolds,[31] imaging the paxillin adhesion sites was only possible by using long acquisition times (5 s), which resulted in background signals. Nevertheless, paxillin-containing adhesion sites can be distinguished around the filaments of the scaffolds. Based on the fluorescence images (Figures 9a−d and S8), more adhesion clusters can be detected on CNT-reinforced scaffolds than on graphene-reinforced scaffolds. This could again result from the different mechanical properties of the scaffolds, but it is also in agreement with cell studies on multiwalled CNTs showing that NIH-3T3 fibroblasts form larger adhesion clusters on CNTs than on graphene.[57]

A further important contribution to cell adhesion is the cytoskeleton, where networks of actin fibers determine cell shape and movements.[58] To investigate cellular actin networks on our scaffolds, we investigated the fluorescence of phalloidin to detect actin fibers. Again, imaging deeply inside the scaffolds was impaired by the strong light absorbance of CNTs and graphene, restricting it to the first 300 μm from the surface. As shown in Figure 9, well-developed actin fibers (in red) are indeed present within the fibroblasts. Furthermore, the cells are polarized and have oriented actin bundles. Figure 9a−c also shows that actin fibers on CNT-reinforced scaffolds (CNTT, AG−CNTT, and CNTT−g) are mainly oriented in the direction of fibroblast protrusions. Although many actin fibers can be detected in cells grown on AG−G (Figure 9d), they are neither well polarized nor elongated like the actin fibers in the cells on CNT-reinforced scaffolds (CNTT, AG−CNTT, and CNTT−g). These results could again originate from the mechanical properties of our materials, similarly to proliferation rate and paxillin clusters.

2.10. ECM-Mimetic Scaffolds. The open porous structure of our scaffolds with large free volumes (>95%) should be highly beneficial for the growth and migration of cells, as the open pores allow the cells to freely migrate and proliferate within the

DOI: 10.1021/acsami.8b17627
ACS Appl. Mater. Interfaces 2019, 11, 5325−5335

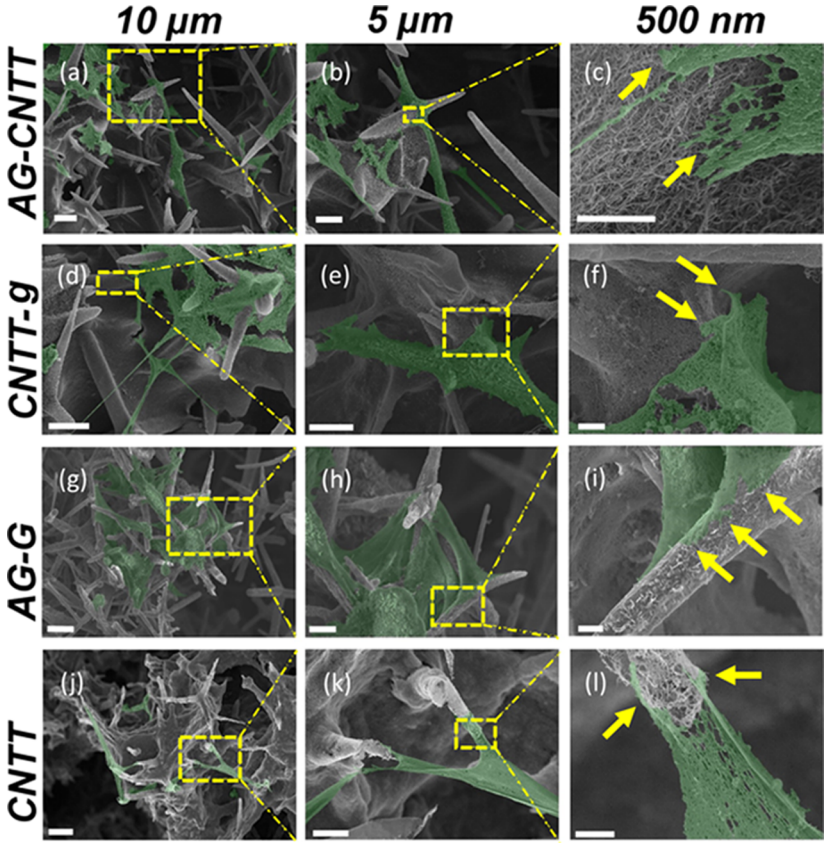

Figure 8. SEM images of REF52wt cells after 7 days of culturing within (a–c) AG–CNTT, (d, e) CNTT–g, (g–i) AG–G, and (j–l) CNTT scaffolds. Left: Medium-sized overview images illustrating the growth of cells between the fibers in different directions and planes; middle: zoomed-in images showing well-stretched cells along the fibers and their elongation; and right: close-up images on the adhesion sites, proving the presence of strong contacts between the materials and the cell membrane (yellow arrows).

scaffolds.[2] Moreover, in contrast to other studies on 3D porous structures, in which the alignment of CNTs[24] or graphene sheets[59] confined the accessibility of cavities, our carbon framework structures provide accessible interconnected pores from all sides (Figure 2). In addition, the hierarchical organization of structural elements, specifically self-entangled CNTs in the form of microtubes, is reminiscent of the hierarchical nano- and microstructure of the ECM. It should therefore in principle be possible to employ our modular design strategy to generate different composition-dependent structural and mechanical features similar to collagen[60] in the ECM. As our scaffolds strongly adsorb proteins, it should also be possible to adsorb adhesion ligands typically present in ECM proteins, such as RGD.[61] In this way, the scaffolds can be modified such that they finally mimic the ECM structurally and biochemically, but with the additional feature of conductivity.

3. CONCLUSIONS

In summary, we have introduced a novel modular design strategy to produce carbon-based scaffolds that mimic the ECM and allow 3D cellular growth. Biocompatibility studies revealed a high proliferation rate of fibroblasts as well as the ability of fibroblasts to develop paxillin-containing adhesion sites. In addition, the cells sprawl and elongate between single filaments of the scaffolds. Tuning electrical conductivity (ca. 0.1–330 S/m), stiffness (ca. 10^{-3}–0.7 MPa), and protein adsorption and porosity (up to ~99%) of the scaffold provides great possibilities for culturing cells. Based on the proven protein adsorption capacity of the scaffolds, they are suitable for biofunctionalization and addition of other biochemical cues. This is particularly relevant in tissue engineering of electrically excitable tissue, e.g., heart tissue, as our scaffolds have tunable electrical conductivity. In addition, the fabrication procedure is very simple and can in principle be adopted to develop 3D assemblies from other low-dimensional nanomaterials (e.g., bioactive ceramic nanoparticles, polymeric nanofibers) by only changing the nanoparticle dispersion, as long as the nanoparticles are connected via strong physical contacts such as entanglement, fusion, or physical locks. This makes the scaffolds promising candidates as conductive ECM-mimetic materials in many applications from regenerative medicine to 3D cell culture.

4. MATERIALS AND METHODS

4.1. Fabrication of 3D Carbon Scaffold Materials. Templates of tetrapod-shaped ZnO were fabricated by a previously developed flame transport synthesis method.[32] The resulting loose powder was pressed into a cylindrical shape (h = 3 mm, d = 6 mm) at a density of 0.3 g/cm^3. The pellets were subsequently sintered for 5 h at 1150 °C to obtain an interconnected 3D ZnO network.[32] This structure is the sacrificial template used for fabrication of carbon-based scaffolds, i.e., free-standing CNTT, AG–CNTT, and AG–G.

For the fabrication of the CNTT scaffolds, the porous ZnO templates were infiltrated with an aqueous dispersion of multiwalled CNTs (1 wt %, CARBOBYK-9810, BYK Additives & Instruments) using a self-built computer-controlled syringe. The length of the CNTs can be on the order of a few micrometers, with diameters in the range of 20–60 nm.[34] After infiltration of ~90 μL of the CNT solution, the samples were dried under ambient conditions for at least 1 h. The process was repeated six times so that CNTs covered the ZnO template.

DOI: 10.1021/acsami.8b17627
ACS Appl. Mater. Interfaces 2019, 11, 5325–5335

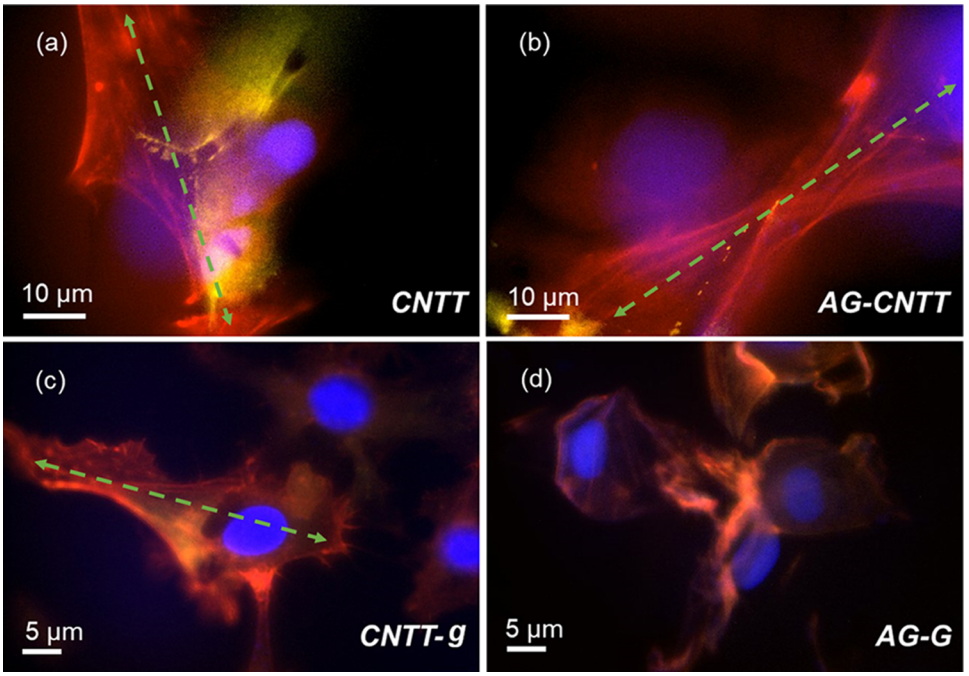

Figure 9. High-magnification fluorescence images of REF52 YFP-paxillin cells on 3D scaffolds: (a) CNTT, (b) AG−CNTT, (c) CNTT−g, and (d) AG−G. YFP-paxillin is mainly distributed in small clusters (YFP; yellow), the nucleus was stained with Hoechst (4′,6-diamidino-2-phenylindole, DAPI; blue), and actin fibers were visualized by phalloidin (red). Fluorescence imaging took place in optical sections approximately between 50 and 100 μm from the surface of the material. Adhesion sites are detectable (a, b) as tiny yellow spots mainly around the tube-shaped filaments of CNTT and AG−CNTT structures. Due to the low intensity and small size of YFP-paxillin (c, d), they are not clearly observed, which is also obscured by red (actin fibers) and blue (nucleus) channels in multichannel images. The green dashed arrows illustrate the protrusion direction of the cells.

Then, the ZnO backbone was removed by immersing the composite in a 1 M HCl solution overnight. The HCl solution was replaced by washing with pure ethanol (five times). Finally, the etched structures were dried in a critical point dryer (EMS 3000) by using the automatic mode. The purge time was set to 15 min to ensure that all ethanol was washed out, leaving freestanding CNTTs.[3]

To alter the CNTT structures further, we added glucose (1 wt %) to the CNT ink used for infiltration. The infiltration into a ZnO template was then repeated four times. After that, the samples were transferred into a quartz tube furnace and heated to 950 °C under argon atmosphere for 2 h. During this process, the ZnO was removed by carbothermal reduction,[45] leading to CNTT−g, which contains both the remnants of the glucose and embedded CNTs.

For the synthesis of AG−CNTT scaffolds, the CNT-coated ZnO templates were exposed to a CVD process, as reported previously.[31] Briefly, the ZnO template was replicated into aerographite at ∼760 °C under a hydrogen and argon atmosphere in the presence of toluene as the source of carbon.[62] Thereby, the CNTs were embedded into the graphite microtubes of aerographite while the ZnO was simultaneously etched by H_2.

A similar process was used to generate composites of graphene and aerographite (AG−G). The graphene ink was made by dispersing graphite flakes (12 mg/mL, Sigma-Aldrich No. 332461) and Triton X-100 stabilization agent (1.7 mg/mL) in deionized water, followed by sonication (Fisherbrand FB15069, Max power 800 W) for 9 h.[63,64] The dispersion was then centrifuged (Sorvall WX100 mounting a TH-641 swinging bucket rotor) at 5k rpm for 1 h to remove the thick flakes. The supernatant (i.e., the top 70%) of the dispersion was then decanted to produce the final graphene ink. In Figure S1, optical absorption spectroscopy (Cary 7000) is used to estimate the flake concentration.[65] The flake concentration in the graphene ink is obtained via the Beer−Lambert law, which links the absorbance $A = \alpha c l$ with the beam path length l (m), the flake concentration c (g/L), and the absorption coefficient α (L/(g m)). The graphene ink was diluted 1:20 with water/Triton X-100. An absorption coefficient of $\alpha \sim 1390$ L/(g m) for the graphene ink at 660 nm was utilized,[66] estimating a graphene flake concentration of ∼0.09 mg/mL, consistent with previous reports of graphene-based inks.[40,67] The spectrum of the graphene ink is mostly featureless due to the linear dispersion of the Dirac electrons, while the peak in the UV region is a signature of the van Hove singularity in the graphene density of states.[68] The ZnO scaffold was infiltrated 50 times to achieve coverage of graphene around the ZnO tetrapods, due to the low concentration of the ink (0.09 mg/mL). After infiltration, the CVD process (see process specification above) was used to embed the graphene flakes into aerographite microtubes and to remove the ZnO template.

4.2. Mechanical and Electrical Characterizations of 3D Carbon Scaffold Materials. Mechanical and electrical characterizations were performed using a self-built setup consisting of a Maerzhaeuser Wetzlar HS 6.3 micromanipulator, which is driven by a stepper motor, a Kern PLE 310-3N precision balance, and a Keithley 6400 source meter. A self-written LabView program controls all components. To avoid any vibration damping, the whole setup is located on a very rigid aluminum plate in a box filled with sand, which is mounted on a vibration-isolated table. Stress−strain curves were measured by placing the sample in between the micromanipulator and the precision balance. For compression tests, the micromanipulator deforms the sample by a user-defined step size. After each step, the program measures the force of the balance after a short settling time has been elapsed. These steps are repeated until the maximum deformation defined by the user is reached. Afterwards, the direction of the deformation is inverted until the micromanipulator comes back to its original position. Finally, the stress−strain curves are evaluated and Young's modulus is determined. With respect to the cyclic compression test, the same procedure was repeated several times. The wait time between each compression step was set to 0 s, and the deformation speed was set to 40 μm/s. To demonstrate the structural integrity, a video was recorded during the long-cycle compression test with a USB camera. Furthermore, the same setup also allows to record the current−voltage characteristics using a Keithley 6400 source meter in the four-wire sense mode. For electrical measurements, the carbon structures were connected to thin copper plates on both sides by using conductive

DOI: 10.1021/acsami.8b17627
ACS Appl. Mater. Interfaces 2019, 11, 5325−5335

silver paste. It is noteworthy that only a thin layer of paste was needed to ensure good electrical connection of the porous material to the measurement setup. Current−voltage curves were measured in a voltage range of up to 5 V. Finally, the resistance was calculated from the obtained data and converted to conductivity to give meaningful values for each structure.

4.3. Cell Culture and Cell Seeding on Scaffolds. Rat embryonic fibroblasts (REF52), both as wild type and stably transfected with YFP-paxillin (REF YFP-Pax),[69] were cultured in Dulbecco's modification of Eagle medium (Biochrom, Germany) at 37 °C, 5% CO_2 at ∼90% humidity. The medium was supplemented with 10% fetal bovine serum (Biochrom, Germany) and 1% penicillin/streptomycin (Sigma-Aldrich, Germany). To expel any traces of remaining zinc from the scaffold fabrication process prior to cell experiments, all samples were immersed in culture medium for 14 days after autoclaving at 121 °C. Shortly before the cell experiments, the cells were immersed in a fresh culture medium, counted with a cell counter (Scepter, Merck Millipore, Germany), and ∼20 000 cells were seeded on each scaffold in 24-well plates. The cells were incubated on the scaffolds for 1, 3, or 7 days.

4.4. Cell Staining. To investigate the cell morphology, proliferation, and adhesion on the scaffolds, cell nuclei were stained with DAPI (Thermo Fisher, Germany), and actin stress fibers were stained with phalloidin (Alexa Fluor 647 phalloidin, Thermo Fisher, Germany). Imaging was carried out using fluorescence microscopy (IX81, Olympus, Germany), and images were processed with cellSens Dimension (Olympus, Germany). For electron microscopy investigations, the cells were fixed by paraformaldehyde (Thermo Fisher, Germany) and dried using critical point drying (EMS 3000). A thin layer of gold was sputtered (Bal-Tec SCD 050, 30 mA, 30 s) onto the sample prior to scanning electron microscopy (SEM) (Ultra Plus Zeiss SEM, 5 kV). The cells in SEM images were highlighted in green (via Adobe Photoshop CC 2017) to distinguish them more easily.

4.5. Viability and Proliferation Assay. The number of living cells on the scaffolds was quantified by a WST-1 proliferation assay after 1, 3, and 7 days of incubation. In this assay, the number of living cells can be acquired from the amount of dye produced via bioreduction of stable tetrazolium salt WST-1 (Sigma-Aldrich, Germany). The amount of formazan is proportional to the number of cells (Cell Proliferation Reagent WST-1 Protocol, Sigma-Aldrich, Germany). The experiments were carried out as follows: After seeding the cells onto each sample (see specification above), the scaffolds were first washed with phosphate buffered saline and then incubated with a WST-1-containing medium for 4 h. The concentration of the formazan dye was quantified by a multiwell spectrophotometer (Bio-Tek μQuant) after removal of the samples from the wells. CNTs tend to react with tetrazolium salts;[70] thus, the proliferation rates were normalized to the absorption of the detected tetrazolium on control samples without cells. The amount of tetrazolium reacting with the scaffolds was determined for each sample as explained in the following: 10 000 cells were cultured for 24 h in 96-well plates prior to adding scaffolds to half of the wells, with the other half serving as scaffold-free control. Then, all of the wells were incubated for an additional time of 4 h with the WST-1 reagent before quantification of the formazan (i.e., product of tetrazolium cell reaction) amount in each well by a multiwell spectrophotometer. The amount of tetrazolium that reacted with the scaffold was calculated for each specimen by subtracting the amount of formazan of scaffold-containing wells from scaffold-free control wells. The difference in absorbance between the scaffolds and controls was used as a correction factor for the data generated with the WST-1 assay.

In addition, the viability of cells was tested according to the ISO 10993 norm. Briefly, 10 000 cells/100 μL REF52 cells were cultured in a 96-well plate for 24 h. For medium extraction, the scaffolds were incubated in a culture medium at 37 °C for 72 h. The cultured cells were incubated with either untreated medium or extracted medium for a further 24 h. To determine cell viability, the colorimetric methylthiazolyldiphenyl-tetrazolium bromide metabolic activity assay (MTT; Sigma-Aldrich, Germany) was used. The cells in untreated medium served as the negative control, and the cells in 20% dimethyl sulfoxide were the positive control. The absorbance was measured at 490 nm (absorption wavelength of formazan) and 600 nm as a reference. The results from the cultured cells with extracted medium were normalized to the values measured for the negative control.

4.6. Protein Adsorption Rate. The protein adsorption rate on the scaffolds was measured by using bovine serum albumin (Pierce; Thermo Fisher, Germany) as a model protein. Protein solution (1 mL, 1 mg/mL) was added per scaffold and incubated at 37 °C in a humidified incubator (CO_2 5%, humidity 95%). After 48 h, nonadhered proteins were carefully removed by a pipette and saved for recording. The scaffolds were washed with saline and incubated for a further 48 h after addition of 1 mL of protein solution. The same procedure was repeated after 48 h. The concentration of protein in the supernatant was measured using a Micro BCA protein assay (Pierce; Thermo Fisher, Germany). To do so, 10 μL of supernatant was mixed with 200 μL of working reagent and incubated for 30 min. The absorbance was measured using a microplate reader (Bio-Tek μQuant) at 570 nm. After calibrating the results with a standard curve provided by the BCA protein assay kit (Pierce; Thermo Fisher, Germany), the protein adsorption rate was calculated by subtracting the residual protein concentration from the initial protein concentration.

■ ASSOCIATED CONTENT

Supporting Information

The Supporting Information is available free of charge on the ACS Publications website at DOI: 10.1021/acsami.8b17627.

Optical absorption spectrum of graphene ink (Figure S1); SEM images of ZnO templates (Figures S2−S4); different 3D carbon tube structures (Figure S5); SEM images of AG−CNTT structures (Figure S6); long-cycle compression test graph of AG−G scaffold (Figure S7); high-magnification fluorescence image of REF52 YFP-paxillin cells (Figure S8); supporting discussion (PDF)

Structural integrity of AG−G scaffold (AVI)

■ AUTHOR INFORMATION

Corresponding Author

*E-mail: cse@tf.uni-kiel.de.

ORCID

Fabian Schütt: 0000-0003-2942-503X
Yogendra Kumar Mishra: 0000-0002-8786-9379
Norbert Stock: 0000-0002-0339-7352
Felice Torrisi: 0000-0002-6144-2916
Christine Selhuber-Unkel: 0000-0002-5051-4822

Notes

The authors declare no competing financial interest.

■ ACKNOWLEDGMENTS

R.A. gratefully acknowledges partial project funding by the Deutsche Forschungsgemeinschaft under contract FOR2093. This project has received funding from the European Union's Horizon 2020 research and innovation programme under grant agreement No. GrapheneCore2 785219. C.S.-U. was supported by the European Research Council (ERC StG 336104 CELLINSPIRED, ERC PoC 768740 CHANNELMAT) and the German Research Foundation (RTG 2154, SFB 1261 project B7). M.T. acknowledges support from the German Academic Exchange Service (DAAD) through a research grant for doctoral candidates (91526555-57048249). The authors acknowledge funding from EPSRC grants EP/P02534X/1, ERC grant 319277 (Hetero2D), the Trinity College, Cambridge, and the Isaac Newton Trust. We also acknowledge Galen Ream for critical proofreading.

DOI: 10.1021/acsami.8b17627
ACS Appl. Mater. Interfaces 2019, 11, 5325−5335

REFERENCES

(1) O'Brien, F. J. Biomaterials & Scaffolds for Tissue Engineering. *Mater. Today* **2011**, *14*, 88−95.
(2) Yang, S.; Leong, K.-F.; Du, Z.; Chua, C.-K. The Design of Scaffolds for Use in Tissue Engineering. Part I. Traditional Factors. *Tissue Eng.* **2001**, *7*, 679−689.
(3) Shoulders, M. D.; Raines, R. T. Collagen Structure and Stability. *Annu. Rev. Biochem.* **2009**, *78*, 929−958.
(4) Friedl, P.; Wolf, K. Plasticity of Cell Migration: A Multiscale Tuning Model. *J. Cell Biol.* **2010**, *188*, 11−19.
(5) Langer, R.; Vacanti, J. P. Tissue Engineering. *Science* **1993**, *260*, 920−926.
(6) Place, E. S.; Evans, N. D.; Stevens, M. M. Complexity in Biomaterials for Tissue Engineering. *Nat. Mater.* **2009**, *8*, 457−470.
(7) Loh, Q. L.; Choong, C. Three-Dimensional Scaffolds for Tissue Engineering Applications: Role of Porosity and Pore Size. *Tissue Eng., Part B* **2013**, *19*, 485−502.
(8) Ganji, Y.; Li, Q.; Quabius, E. S.; Böttner, M.; Selhuber-Unkel, C.; Kasra, M. Cardiomyocyte Behavior on Biodegradable Polyurethane/Gold Nanocomposite Scaffolds under Electrical Stimulation. *Mater. Sci. Eng., C* **2016**, *59*, 10−18.
(9) Potse, M.; Dubé, B.; Vinet, A. Cardiac Anisotropy in Boundary-Element Models for the Electrocardiogram. *Med. Biol. Eng. Comput.* **2009**, *47*, 719−729.
(10) Fang, B.; Yang, J.; Chen, C.; Zhang, C.; Chang, D.; Xu, H.; Gao, C. Carbon Nanotubes Loaded on Graphene Microfolds as Efficient Bifunctional Electrocatalysts for the Oxygen Reduction and Oxygen Evolution Reactions. *ChemCatChem* **2017**, *9*, 4520−4528.
(11) Li, Z.; Liu, Z.; Sun, H.; Gao, C. Superstructured Assembly of Nanocarbons: Fullerenes, Nanotubes, and Graphene. *Chem. Rev.* **2015**, *115*, 7046−7117.
(12) Lekawa-Raus, A.; Patmore, J.; Kurzepa, L.; Bulmer, J.; Koziol, K. Electrical Properties of Carbon Nanotube Based Fibers and Their Future Use in Electrical Wiring. *Adv. Funct. Mater.* **2014**, *24*, 3661−3682.
(13) Sahebian, S.; Zebarjad, S. M.; vahdati Khaki, J.; Lazzeri, A. A Study on the Dependence of Structure of Multi-Walled Carbon Nanotubes on Acid Treatment. *J. Nanostruct. Chem.* **2015**, *5*, 287−293.
(14) Aliofkhazraei, M.; Ali, N.; Milne, W. I.; Ozkan, C. S.; Mitura, S.; Gervasoni, J. L. *Graphene Science Handbook: Electrical and Optical Properties*; CRC Press, 2016; p 715.
(15) Chen, J. H.; Jang, C.; Xiao, S.; Ishigami, M.; Fuhrer, M. S. Intrinsic and Extrinsic Performance Limits of Graphene Devices on SiO2. *Nat. Nanotechnol.* **2008**, *3*, 206−209.
(16) Gorityala, B. K.; Ma, J.; Wang, X.; Chen, P.; Liu, X. W. Carbohydrate Functionalized Carbon Nanotubes and Their Applications. *Chem. Soc. Rev.* **2010**, *39*, 2925−2934.
(17) Bhunia, S. K.; Saha, A.; Maity, A. R.; Ray, S. C.; Jana, N. R. Carbon Nanoparticle-Based Fluorescent Bioimaging Probes. *Sci. Rep.* **2013**, *3*, 1473.
(18) Fabbro, A.; Scaini, D.; León, V.; Vázquez, E.; Cellot, G.; Privitera, G.; Lombardi, L.; Torrisi, F.; Tomarchio, F.; Bonaccorso, F.; Bosi, S.; Ferrari, A. C.; Ballerini, L.; Prato, M. Graphene-Based Interfaces Do Not Alter Target Nerve Cells. *ACS Nano* **2016**, *10*, 615−623.
(19) Call, T. P.; Carey, T.; Bombelli, P.; Lea-Smith, D. J.; Hooper, P.; Howe, C. J.; Torrisi, F. Platinum-Free, Graphene Based Anodes and Air Cathodes for Single Chamber Microbial Fuel Cells. *J. Mater. Chem. A* **2017**, *5*, 23872−23886.
(20) Li, N.; Zhang, Q.; Gao, S.; Song, Q.; Huang, R.; Wang, L.; Liu, L.; Dai, J.; Tang, M.; Cheng, G. Three-Dimensional Graphene Foam as a Biocompatible and Conductive Scaffold for Neural Stem Cells. *Sci. Rep.* **2013**, *3*, 1604.
(21) Mooney, E.; Dockery, P.; Greiser, U.; Murphy, M.; Barron, V. Carbon Nanotubes and Mesenchymal Stem Cells: Biocompatibility, Proliferation and Differentiation. *Nano Lett.* **2008**, *8*, 2137−2143.
(22) Yang, S. T.; Luo, J.; Zhou, Q.; Wang, H. Pharmacokinetics, Metabolism and Toxicity of Carbon Nanotubes for Bio-Medical Purposes. *Theranostics* **2012**, *2*, 271−282.
(23) Jia, G.; Wang, H.; Yan, L.; Wang, X.; Pei, R.; Yan, T.; Zhao, Y.; Guo, X. Cytotoxicity of Carbon Nanomaterials: Single-Wall Nanotube, Multi-Wall Nanotube, and Fullerene. *Environ. Sci. Technol.* **2005**, *39*, 1378−1383.
(24) Correa-Duarte, M. A.; Wagner, N.; Rojas-Chapana, J.; Morsczeck, C.; Thie, M.; Giersig, M. Fabrication and Biocompatibility of Carbon Nanotube-Based 3D Networks as Scaffolds for Cell Seeding and Growth. *Nano Lett.* **2004**, *4*, 2233−2236.
(25) Edwards, S. L.; Church, J. S.; Werkmeister, J. A.; Ramshaw, J. A. M. Tubular Micro-Scale Multiwalled Carbon Nanotube-Based Scaffolds for Tissue Engineering. *Biomaterials* **2009**, *30*, 1725−1731.
(26) Liu, Y.; Zhao, Y.; Sun, B.; Chen, C. Understanding the Toxicity of Carbon Nanotubes. *Acc. Chem. Res.* **2013**, *46*, 702−713.
(27) Cohen-Karni, T.; Qing, Q.; Li, Q.; Fang, Y.; Lieber, C. M. Graphene and Nanowire Transistors for Cellular Interfaces and Electrical Recording. *Nano Lett.* **2010**, *10*, 1098−1102.
(28) Akhavan, O.; Ghaderi, E.; Shahsavar, M. Graphene Nanogrids for Selective and Fast Osteogenic Differentiation of Human Mesenchymal Stem Cells. *Carbon* **2013**, *59*, 200−211.
(29) Shin, S. R.; Li, Y. C.; Jang, H. L.; Khoshakhlagh, P.; Akbari, M.; Nasajpour, A.; Zhang, Y. S.; Tamayol, A.; Khademhosseini, A. Graphene-Based Materials for Tissue Engineering. *Adv. Drug Delivery Rev.* **2016**, *105*, 255−274.
(30) Smith, S. C.; Ahmed, F.; Gutierrez, K. M.; Frigi Rodrigues, D. A Comparative Study of Lysozyme Adsorption with Graphene, Graphene Oxide, and Single-Walled Carbon Nanotubes: Potential Environmental Applications. *Chem. Eng. J.* **2014**, *240*, 147−154.
(31) Mecklenburg, M.; Schuchardt, A.; Mishra, Y. K.; Kaps, S.; Adelung, R.; Lotnyk, A.; Kienle, L.; Schulte, K. Aerographite: Ultra Lightweight, Flexible Nanowall, Carbon Microtube Material with Outstanding Mechanical Performance. *Adv. Mater.* **2012**, *24*, 3486−3490.
(32) Mishra, Y. K.; Kaps, S.; Schuchardt, A.; Paulowicz, I.; Jin, X.; Gedamu, D.; Freitag, S.; Claus, M.; Wille, S.; Kovalev, A.; Gorb, S. N.; Adelung, R. Fabrication of Macroscopically Flexible and Highly Porous 3D Semiconductor Networks from Interpenetrating Nanostructures by a Simple Flame Transport Approach. *Part. Part. Syst. Charact.* **2013**, *30*, 775−783.
(33) Lamprecht, C.; Taale, M.; Paulowicz, I.; Westerhaus, H.; Grabosch, C.; Schuchardt, A.; Mecklenburg, M.; Böttner, M.; Lucius, R.; Schulte, K.; Adelung, R.; Selhuber-Unkel, C. A Tunable Scaffold of Microtubular Graphite for 3D Cell Growth. *ACS Appl. Mater. Interfaces* **2016**, *8*, 14980−14985.
(34) Mouw, J. K.; Ou, G.; Weaver, V. M. Extracellular Matrix Assembly: A Multiscale Deconstruction. *Nat. Rev. Mol. Cell Biol.* **2014**, *15*, 771−785.
(35) Schütt, F.; Signetti, S.; Krüger, H.; Röder, S.; Smazna, D.; Kaps, S.; Gorb, S. N.; Mishra, Y. K.; Pugno, N. M.; Adelung, R. Hierarchical Self-Entangled Carbon Nanotube Tube Networks. *Nat. Commun.* **2017**, *8*, No. 1215.
(36) Feng, X.; Feng, L.; Jin, M.; Zhai, J.; Jiang, L.; Zhu, D. Reversible Super-Hydrophobicity to Super-Hydrophilicity Transition of Aligned ZnO Nanorod Films. *J. Am. Chem. Soc.* **2004**, *126*, 62−63.
(37) Chen, H.-K. Kinetic Study on the Carbothermic Reduction of Zinc Oxide. *Scand. J. Metall.* **2001**, *30*, 292−296.
(38) Zhao, J.; Xing, B.; Yang, H.; Pan, Q.; Li, Z.; Liu, Z. Growth of Carbon Nanotubes on Graphene by Chemical Vapor Deposition. *New Carbon Mater.* **2016**, *31*, 31−36.
(39) Ferrari, A. C.; Robertson, J. Resonant Raman Spectroscopy of Disordered, Amorphous, and Diamondlike Carbon. *Phys. Rev. B: Condens. Matter Mater. Phys.* **2001**, *64*, 075414.
(40) Carey, T.; Cacovich, S.; Divitini, G.; Ren, J.; Mansouri, A.; Kim, J. M.; Wang, C.; Ducati, C.; Sordan, R.; Torrisi, F. Fully Inkjet-Printed Two-Dimensional Material Field-Effect Heterojunctions for Wearable and Textile Electronics. *Nat. Commun.* **2017**, *8*, 1202.
(41) Ferrari, A. C.; Meyer, J. C.; Scardaci, V.; Casiraghi, C.; Lazzeri, M.; Mauri, F.; Piscanec, S.; Jiang, D.; Novoselov, K. S.; Roth, S.; et al. Raman Spectrum of Graphene and Graphene Layers. *Phys. Rev. Lett.* **2006**, *97*, 187401.

DOI: 10.1021/acsami.8b17627
ACS Appl. Mater. Interfaces 2019, 11, 5325−5335

(42) Ferrari, A.; Robertson, J. Interpretation of Raman Spectra of Disordered and Amorphous Carbon. *Phys. Rev. B: Condens. Matter Mater. Phys.* **2000**, *61*, 14095−14107.
(43) Cuscó, R.; Alarcón-Lladó, E.; Ibáñez, J.; Artús, L.; Jiménez, J.; Wang, B.; Callahan, M. Temperature Dependence of Raman Scattering in ZnO. *Phys. Rev. B: Condens. Matter Mater. Phys.* **2007**, *75*, 165202.
(44) Fan, H.; Wang, L.; Zhao, K.; Li, N.; Shi, Z.; Ge, Z.; Jin, Z. Fabrication, Mechanical Properties, and Biocompatibility of Graphene-Reinforced Chitosan Composites. *Biomacromolecules* **2010**, *11*, 2345−2351.
(45) Ahadian, S.; Ramón-Azcón, J.; Estili, M.; Liang, X.; Ostrovidov, S.; Shiku, H.; Ramalingam, M.; Nakajima, K.; Sakka, Y.; Bae, H. H.; Matsue, T.; Khademhosseini, A. Hybrid Hydrogels Containing Vertically Aligned Carbon Nanotubes with Anisotropic Electrical Conductivity for Muscle Myofiber Fabrication. *Sci. Rep.* **2015**, *4*, 4271.
(46) Shi, X.; Sitharaman, B.; Pham, Q. P.; Liang, F.; Wu, K.; Edward Billups, W.; Wilson, L. J.; Mikos, A. G. Fabrication of Porous Ultra-Short Single-Walled Carbon Nanotube Nanocomposite Scaffolds for Bone Tissue Engineering. *Biomaterials* **2007**, *28*, 4078−4090.
(47) Chen, Z.; Ren, W.; Gao, L.; Liu, B.; Pei, S.; Cheng, H. M. Three-Dimensional Flexible and Conductive Interconnected Graphene Networks Grown by Chemical Vapour Deposition. *Nat. Mater.* **2011**, *10*, 424−428.
(48) Zhao, G.; Zhang, X.; Lu, T. J.; Xu, F. Recent Advances in Electrospun Nanofibrous Scaffolds for Cardiac Tissue Engineering. *Adv. Funct. Mater.* **2015**, *25*, 5726−5738.
(49) Zuo, G.; Kang, S. G.; Xiu, P.; Zhao, Y.; Zhou, R. Interactions between Proteins and Carbon-Based Nanoparticles: Exploring the Origin of Nanotoxicity at the Molecular Level. *Small* **2013**, *9*, 1546−1556.
(50) Suh, C. W.; Kim, M. Y.; Choo, J. B.; Kim, J. K.; Kim, H. K.; Lee, E. K. Analysis of Protein Adsorption Characteristics to Nano-Pore Silica Particles by Using Confocal Laser Scanning Microscopy. *J. Biotechnol.* **2004**, *112*, 267−277.
(51) Prager-Khoutorsky, M.; Lichtenstein, A.; Krishnan, R.; Rajendran, K.; Mayo, A.; Kam, Z.; Geiger, B.; Bershadsky, A. D. Fibroblast Polarization Is a Matrix-Rigidity-Dependent Process Controlled by Focal Adhesion Mechanosensing. *Nat. Cell Biol.* **2011**, *13*, 1457−1465.
(52) El-Mohri, H.; Wu, Y.; Mohanty, S.; Ghosh, G. Impact of Matrix Stiffness on Fibroblast Function. *Mater. Sci. Eng., C* **2017**, *74*, 146−151.
(53) Sun, Y.; Chen, C. S.; Fu, J. Forcing Stem Cells to Behave: A Biophysical Perspective of the Cellular Microenvironment. *Annu. Rev. Biophys.* **2012**, *41*, 519−542.
(54) Moreno-Arotzena, O.; Borau, C.; Movilla, N.; Vicente-Manzanares, M.; García-Aznar, J. M. Fibroblast Migration in 3D Is Controlled by Haptotaxis in a Non-Muscle Myosin II-Dependent Manner. *Ann. Biomed. Eng.* **2015**, *43*, 3025−3039.
(55) Turner, C. E. Paxillin and Focal Adhesion Signalling. *Nat. Cell Biol.* **2000**, *2*, E231−E236.
(56) Chiu, C.-L.; Aguilar, J. S.; Tsai, C. Y.; Wu, G.; Gratton, E.; Digman, M. M. A.; Kuo, J.; Han, X.; Hsiao, C.; Iii, J. Y.; et al. Nanoimaging of Focal Adhesion Dynamics in 3D. *PLoS One* **2014**, *9*, e99896.
(57) Ryoo, S. R.; Kim, Y. K.; Kim, M. H.; Min, D. H. Behaviors of NIH-3T3 Fibroblasts on Graphene/Carbon Nanotubes: Proliferation, Focal Adhesion, and Gene Transfection Studies. *ACS Nano* **2010**, *4*, 6587−6598.
(58) Cooper, G. M. *The Cell: A Molecular Approach*; ASM Press, 2000; Vol. *10*.
(59) Serrano, M. C.; Patiño, J.; García-Rama, C.; Ferrer, M. L.; Fierro, J. L. G.; Tamayo, A.; Collazos-Castro, J. E.; Del Monte, F.; Gutiérrez, M. C. 3D Free-Standing Porous Scaffolds Made of Graphene Oxide as Substrates for Neural Cell Growth. *J. Mater. Chem. B* **2014**, *2*, 5698−5706.
(60) Avery, N. C.; Bailey, A. J.; Fratzl, P. *Collagen: Structure and Mechanics*; Springer, 2008.
(61) LeBaron, R. G.; Athanasiou, K. A. Extracellular Matrix Cell Adhesion Peptides: Functional Applications in Orthopedic Materials. *Tissue Eng.* **2000**, *6*, 85−103.
(62) Marx, J.; Lewke, M. R. D.; Smazna, D.; Mishra, Y. K.; Adelung, R.; Schulte, K.; Fiedler, B. Processing, Growth Mechanism and Thermodynamic Calculations of Carbon Foam with a Hollow Tetrapodal Morphology − Aerographite. *Appl. Surf. Sci.* **2019**, *470*, 535−542.
(63) Wang, F.; Torrisi, F.; Jiang, Z.; Popa, D.; Hasan, T.; Sun, Z.; Cho, W.; Ferrari, A. C. Graphene Passively Q-Switched Two-Micron Fiber Lasers. In *Conference on Lasers and Electro-Optics (CLEO); OSA Technical Digest* (Optical Society of America): San Jose, CA, 2012; p JW2A 72.
(64) Purdie, D. G.; Popa, D.; Wittwer, V. J.; Jiang, Z.; Bonacchini, G.; Torrisi, F.; Milana, S.; Lidorikis, E.; Ferrari, A. C. Few-Cycle Pulses from a Graphene Mode-Locked All-Fiber Laser. *Appl. Phys. Lett.* **2015**, *106*, 253101.
(65) Bianchi, V.; Carey, T.; Viti, L.; Li, L.; Linfield, E. H.; Davies, A. G.; Tredicucci, A.; Yoon, D.; Karagiannidis, P. G.; Lombardi, L.; Tomarchio, F.; Ferrari, A. C.; Torrisi, F.; Vitiello, M. S. Terahertz Saturable Absorbers from Liquid Phase Exfoliation of Graphite. *Nat. Commun.* **2017**, *8*, 15763.
(66) Lotya, M.; Hernandez, Y.; King, P. J.; Smith, R. J.; Nicolosi, V.; Karlsson, L. S.; Blighe, F. M.; De, S.; Wang, Z.; McGovern, I. T.; Duesberg, G. S.; Coleman, J. N. Liquid Phase Production of Graphene by Exfoliation of Graphite in Surfactant/Water Solutions. *J. Am. Chem. Soc.* **2009**, *131*, 3611−3620.
(67) Carey, T.; Jones, C.; Le Moal, F.; Deganello, D.; Torrisi, F. Spray Coating Thin Films on Three-Dimensional Surfaces for a Semi-Transparent Capacitive Touch Device. *ACS Appl. Mater. Interfaces* **2018**, *10*, 19948−19956.
(68) Kravets, V. G.; Grigorenko, A. N.; Nair, R. R.; Blake, P.; Anissimova, S.; Novoselov, K. S.; Geim, A. K. Spectroscopic Ellipsometry of Graphene and an Exciton-Shifted van Hove Peak in Absorption. *Phys. Rev. B: Condens. Matter Mater. Phys.* **2010**, *81*, 155413.
(69) Selhuber-Unkel, C.; Erdmann, T.; López-García, M.; Kessler, H.; Schwarz, U. S.; Spatz, J. P. Cell Adhesion Strength Is Controlled by Intermolecular Spacing of Adhesion Receptors. *Biophys. J.* **2010**, *98*, 543−551.
(70) Wörle-Knirsch, J. M.; Pulskamp, K.; Krug, H. F. Oops They Did It Again! Carbon Nanotubes Hoax Scientists in Viability Assays. *Nano Lett.* **2006**, *6*, 1261−1268.

DOI: 10.1021/acsami.8b17627
ACS Appl. Mater. Interfaces 2019, 11, 5325−5335